# Two-Dimensionally Grown Single-Crystal Silicon Nanosheets with Tunable Visible-Light Emissions

**Sung Wook Kim,[†] Jaejun Lee,[†] Ji Ho Sung,[‡] Dong-jae Seo,[†] Ilsoo Kim,[†] Moon-Ho Jo,[‡] Byoung Wook Kwon,[§] Won Kook Choi,[§] and Heon-Jin Choi[†,*]**

[†]Global E[3] Institute and Department of Materials Science and Engineering, Yonsei University, Seoul 120-749, Korea, [‡]Center for Artificial Low Dimensional Electronic Systems (IBS) and Department of Materials Science and Engineering, Pohang University of Science and Technology, Pohang 790-784, Korea, and [§]Future Convergence Research Divisions, Korea Institute of Science and Technology, Seoul 130-650, Korea. S.W. K. and H. J. C. are responsible for all phases of the research; J.J.L., D.J.S. and I.S.K. helped with synthesis and characterization of thickness controlled SiNSs; J.H.S. and J.H.M. measured photocurrent; B.W.K. and W.K.C. fabricated hybrid OLED devices and measured electroluminescence.

**ABSTRACT** Since the discovery of graphene, growth of two-dimensional (2D) nanomaterials has greatly attracted attention. However, spontaneous growth of atomic two-dimensional (2D) materials is limitedly permitted for several layered-structure crystals, such as graphene, $MoS_2$, and *h*-BN, and otherwise it is notoriously difficult. Here we report the gas-phase 2D growth of silicon (Si), that is cubic in symmetry, *via* dendritic growth and an interdendritic filling mechanism and to form Si nanosheets (SiNSs) of 1 to 13 nm in thickness. Thin SiNSs show strong thickness-dependent photoluminescence in visible range including red, green, and blue (RGB) emissions with the associated band gap energies ranging from 1.6 to 3.2 eV; these emission energies were greater than those from Si quantum dots (SiQDs) of the similar sizes. We also demonstrated that electrically driven white, as well as blue, emission in a conventional organic light-emitting diode (OLED) geometry with the SiNS assembly as the active emitting layers. Tunable light emissions in visible range in our observations suggest practical implications for novel 2D Si nanophotonics.

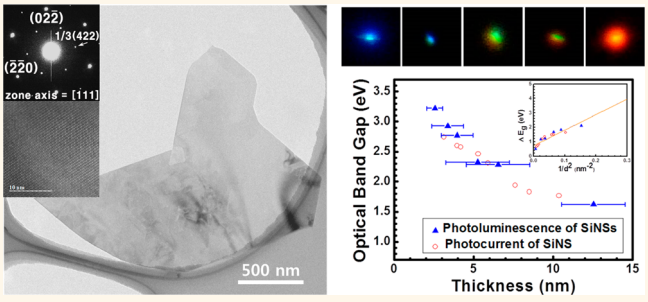


**KEYWORDS:** Si nanosheets · 2D growth · thickness-dependent photoluminescence · tunable emission

Significant efforts have been made to grow two-dimensional (2D) nanostructures of various materials. It is known that the spontaneous growth of 2D nanostructures generally requires a layered or anisotropic crystal structure and is thus limited in materials such as graphene, *h*-BN and $MoS_2$.[1−3] The graphene has strong covalent bonds in a layer and weak van der Waals bonds between layers due to 2D honeycomb lattice structures bonded with a single layer of $sp^2$-hybridized carbon atoms.[4,5] This anisotropic structure leads 2D growth and make possible to prepare 2D nanostructures.[6] The *h*-BN and $MoS_2$ also have the structures analogues of graphenes,[7,8] and thus various synthesis methods for graphene, *h*-BN and $MoS_2$ can be developed, including micromechanical cleavage, epitaxial growth, chemical vapor deposition, substrate-free gas phase synthesis, *etc.*[9,10] Meanwhile, 2D nanostructures of materials such as complementary metal-oxide-semiconductor (CMOS)-compatible Si would be advantageous for many applications. However, Si has isotropic, cubic structures and, thus, is not expected to exhibit 2D growth. Recently, chemical methods using Si-organics or Si-carbon have been studied for the fabrication of 2D Si nanostructures.[11−14] With these methods, 2D Si hybrid nanostructures composed of Si-organic materials could be prepared. However, the free-standing, single-crystal 2D Si nanostructures that are essential to address the intrinsic properties of these novel nanostructures as well as use them as building blocks for many applications cannot be prepared with the methods. Herein, we report the controlled growth of free-standing, single-crystal 2D Si nanostructures, that is,

* Address correspondence to hjc@yonsei.ac.kr.

Received for review March 27, 2014 and accepted May 23, 2014.

**Published online May 23, 2014**
**10.1021/nn501683f**

of SiNSs with thicknesses as low as 1 nm. These SiNSs exhibited tunable emissions at visible wavelengths.

## RESULTS AND DISCUSSION

We grew SiNSs through chemical vapor deposition (CVD) using $SiCl_4$ as the Si precursor and $H_2$ as the carrier gas.[15] We systematically investigated the growth behavior of such SiNSs and found that a high flow rate of $H_2$ is essential for the 2D growth. The supersaturation of the reactant (*i.e.*, the amount of $SiCl_4$ in the $H_2$ carrier gas) was another important parameter for the growth. The growth of the Si crystals as a function of the two critical parameters (*i.e.*, the flow rate of $H_2$ and $SiCl_4/H_2$ ratio) is depicted in Figure S1 (Supporting Information). As shown in the figure, particles of different shapes, quasi-nanosheets with nanowires, smooth nanosheets, and surface-roughened nanosheets grew under different conditions. The optimum conditions for the 2D growth of SiNSs were an $H_2$ flow rate of 2000 to 4000 sccm and a $SiCl_4/H_2$ supersaturation ratio of $4 \times 10^{-3}$ to $1 \times 10^{-2}$.

It was found that the SiNSs grew in three stages (Figure 1a). The first stage was one-dimensional (1D) seed growth, that is, the growth of 1D Si nanowires along the ⟨110⟩ directions; these protruded from the substrate and were free-standing (Figure 1b). The second stage was 2D sheet growth, that is, the branching of the seed nanowires along the six ⟨110⟩ directions normal to the [111] direction and the formation of 2D dendrites, followed by the filling of the spaces between the dendrites along the side face in the ⟨112⟩ directions (Figure 1c–f). Finally, the third stage was the thickening of the SiNSs along the ⟨111⟩ directions. It was noticed that the widening of the SiNSs by the formation of dendrites and the filling of the interdendritic space occurred quickly while the thickening progressed very slowly. It was also found that there are no interfacial Si layers between the substrate and the SiNSs or Si nanoparticles or other Si debris on the substrates (Figure S2, Supporting Information). High-resolution transmission electron microscopy (HRTEM) images showed that all the SiNSs were composed of single-crystal, pure Si. No defects such as dislocations or stacking faults were noticed in the HRTEM images (Figure 1g and Figure S3, Supporting Information). The crystal structure and growth direction of the SiNSs was found to cubic structure, and ⟨111⟩ along the thickness and ⟨110⟩ along the diameter, respectively (Figure S4, Supporting Information, and Figure 1G).

Taking into account the growth behavior and its relation to the processing parameters, it is clear that $H_2$ flowing at a high rate suppresses the growth of Si

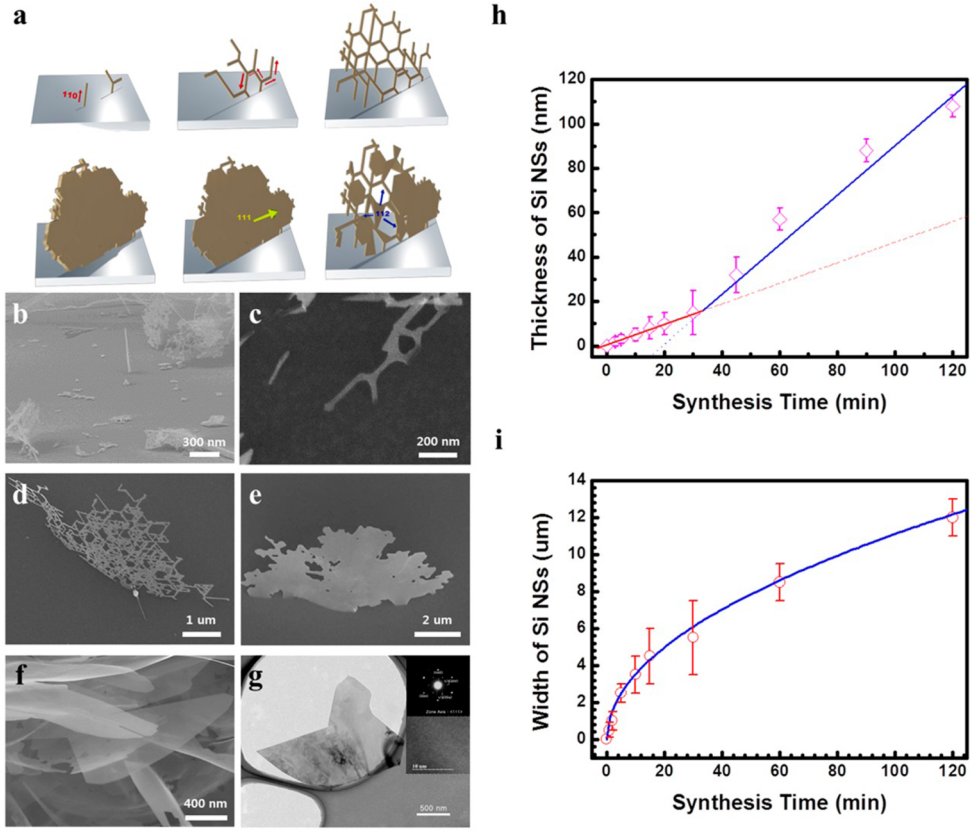


**Figure 1. Synthesis of thickness-controlled SiNSs. (a) Schematic illustration of the growth mechanism of the SiNSs. (b–f) SEM images showing the different growth stages of SiNSs. (g) TEM image and SAD pattern (inset) of SiNSs showing single crystallinity without defects. (h) Average thickness of the SiNSs as a function of the growth time. (i) Average width of the SiNSs as a function of the growth time.**

in the ⟨111⟩ directions. It is known that $H_2$ passivates the Si surface or causes Si atoms to desorb from the surface.[16−18] The passivation process stabilizes the surface by reducing the surface energy. Thus, passivation and/or desorption will suppress the growth of Si at the surface. It should be noted that whether passivation and/or desorption occurs will dependent on the nature of the surface. In the case of (111) surfaces, the Si atoms that are adsorbed onto the surface only form a bond with the Si atoms on the surface and thus can be easily made to desorb by $H_2$, resulting in the formation of byproducts (*e.g.*, Si−H−Cl). Meanwhile, the surface is readily passivated by $H_2$. As a result, it becomes atomically smooth and does not allow Si atoms to be adsorbed onto it.[19] On the other hand, in the case of (110) surfaces, the adsorbed Si atoms can bond with the Si atoms beneath the surface as well as those on the sides of the surface and are thus more stable with respect to desorption owing to $H_2$. Moreover, the Si atoms on (110) surfaces act as steps and help the surface adsorption process (Figure S3, Supporting Information). A high $H_2$ flow rate can further enforce the passivation and desorption by increasing the number of effective collisions or impingements of $H_2$ molecules on the surface. This can strongly suppresses growth in the ⟨111⟩ directions.

The 1D growth of Si nanowires from Si substrates during the initial seeding stage is of interest because it occurs without requiring a metal catalyst. The suppression of crystal growth in the ⟨111⟩ directions and the thermodynamic stability of the 1D nanostructures that grow in the ⟨110⟩ directions might be responsible for the growth of the Si nanowires in the ⟨110⟩ directions in the absence of a catalyst. The 2D growth in the ⟨110⟩ directions that follows occurs quickly, owing to the dendritic branching and the filling of the interdendritic space, as shown in Figure 1c−e. It is known that low supersaturation induces diffusion-limited aggregation (DLA) and leads to dendritic growth in many types of crystals.[20−22] The supersaturation of $SiCl_4$ was low enough to induce DLA in the case of the Si nanowires and to lead to dendritic growth. The preferential dendritic growth along the ⟨110⟩ directions can be thermodynamically attributed to the minimization of the total surface energy owing to the exposure of the (111) plane.[23,24] The subsequent planar filling of the spaces in the ⟨112⟩ directions in the dendrites and the formation of sheets can be attributed to the minimization of the total surface energy owing to the decrease in the specific surface area of the dendritic structures. This filling process can also be attributed to the selective condensation of vapors on the concave corner sites between the branches of the networks, where the chemical potential (*i.e.*, the equilibrium partial vapor pressure) is lower than that at the flat surface sites, according to the Gibbs−Thomson relation.[25] It should be noted that single crystallinity is maintained throughout the growth process, resulting in single-crystal SiNSs that are free of defects or faults (Figure 1g and Figure S4, Supporting Information).

We could control the size of the SiNSs. Under low supersaturation conditions (*e.g.*, for a $SiCl_4/H_2$ gas ratio of $5 \times 10^{-3}$), the thickening rate in the ⟨111⟩ directions could be controlled to approximately 1 nm/min, as shown in Figure 1h. The low supersaturation state makes the supply of $SiCl_4$ the rate-determining step for the thickening process and allows for the control of the thickening rate on the basis of the amount of $SiCl_4$ supplied. The average nominal thickness of the SiNSs could thus be reliably controlled from approximately 1 to 100 nm. Figure 1h also shows that the thickening rate was different in the two regimes of the growth process. In the first regime (*i.e.*, for growth times of up to 30 min), the thickening rate was quite low. It subsequently increased in the second regime. This may be due to the faceting of the ⟨111⟩ surfaces during the second regime. We found that the ⟨111⟩ surfaces of the SiNSs were smooth in the early stage, but became slightly faceted in the later stage (Figure S5, Supporting Information). The existence of such faceted surfaces could be the reason for the relatively fast thickening in the second regime. Meanwhile, the widening of the SiNSs was proportional to the square root of the growth time. In the low-supersaturation state, the supply of $SiCl_4$ is the rate-limiting step for the widening process, and therefore, the rate of increase of the surface area (A) would be constant when the amount of $SiCl_4$ supplied was constant with time. Therefore, the diameter of the SiNSs was proportional to the square root of the growth time since $A$ ($= \pi d^2/4$) $\propto at$, and, therefore, $d \propto bt^{1/2}$, where $d$ is the diameter of the SiNSs, $a$ and $b$ are constants, and $t$ is the growth time.

Interestingly, the SiNSs exhibited tunable emissions in the visible range. Figure 2 shows the photoluminescence (PL) spectra of the SiNSs at room temperature. The wavelengths of the PL spectra for SiNSs synthesized for different growth times extended over the visible region, corresponding to violet (385 nm), blue (430 nm), green/yellow (550 nm), and red (765 nm) emissions. It is likely that that the thickness of the SiNSs (see Figure 1) is the reason for the change in the color of the emissions, because no other significant physical or chemical changes were observed in the SiNSs with increases in the growth time. Emissions from pure Si nanostructures (*e.g.*, Si quantum dots (SiQDs) and porous Si) originate owing to exitonic recombinations (*i.e.*, the formation of exitons by the recombination of electrons in the conduction band and holes in the valence band). Another reason could be the trapping of charge carriers at the surfaces followed by their recombination (*i.e.*, the recombination of electrons and holes trapped in a surface state).[26] In the former case, the wavelengths of the emissions would be affected by the size of Si nanostructures; in the latter case, they

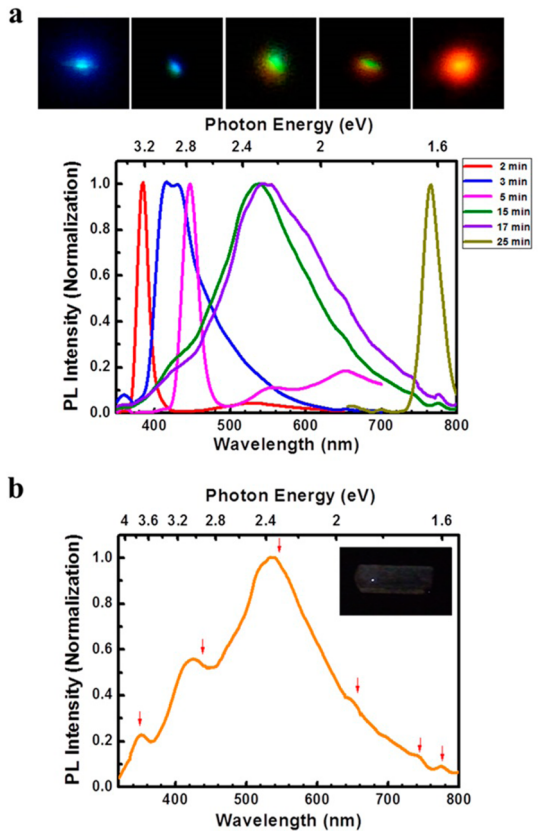


**Figure 2. Full-color light emission from the SiNSs. (a) Real-color images of the thickness-controlled SiNSs (emissions ranging from blue to red) and corresponding PL spectra as a function of growth time. (b) White-light emission and PL spectrum of mixed SiNSs.**

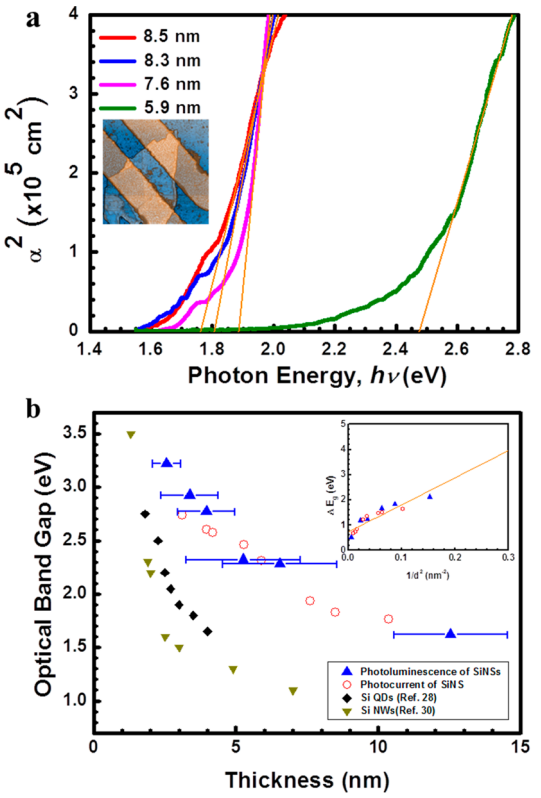


**Figure 3. Measurement of light absorption and the optical band gap energy of the individual SiNSs. (a) Squared absorption coefficient of the thickness-controlled SiNSs as a function of the incident photon energy. The inset shows a photograph of the single-SiNS photodetector device. (b) Optical band gap of the SiNSs as a function of the thickness determined from photoluminescence and photocurrent measurements. The inset shows the optical band gap as a function of thickness$^{1/2}$.**

would not. Therefore, Figure 2 indicates that the excitonic recombinations were the cause of the emissions. This also explains the maximum half width of the PL spectrum, shown in Figure 2; it increases as the spectrum is red-shifted. As shown in Figure 1, the thickness distribution of the SiNSs became wider with an increase in the growth time; this could be the reason for the widening of the PL spectrum. One exception to this correlation is the narrow bandwidth observed in the case of the red emission (wavelength of 765 nm for an average thickness of 13 $\pm$ 3 nm), even though the thickness distribution of the SiNSs in this case was quite wide. This phenomenon may be attributable to a decrease in the spectrum intensity at wavelengths longer than those corresponding to red emissions as the thickness approaches the threshold value for emissions in the visible range.[27,28]

We further characterized the optical properties of the SiNSs by measuring the photocurrent induced in individual SiNSs. Unlike SiQDs, the SiNSs were micrometer sized in width. Thus, it was possible to fabricate photocurrent devices with electrodes to determine the optical properties of the individual SiNSs. Figure 3a shows the photocurrent measured from the SiNSs. The SiNSs exhibited a photocurrent response when illuminated with radiation of specific wavelengths. Therefore, their band gap could be determined as a function of their thickness. The measurements indicate that the absorption edge and optical band gap varied from 1.7 to 2.5 eV for nominal thicknesses of 5 to 9 nm.

Figure 3b plots the optical band gap of the SiNSs as a function of their thickness as determined from the PL and photocurrent measurements. The data from the different measurements matched well; although the PL data is an ensemble of emissions from many SiNSs, while the photocurrent data represents the absorption and current responses of individual SiNSs. It should be noted that the band gap energies are proportional to $1/t^2$, where $t$ is the thickness (see inset in Figure 3b), in keeping with the quantum confinement effect.[29] It should also be noted that the variation in the band gap was quite large. The optical band gaps of SiQDs and Si nanowires (SiNWs) vary with their surface states and size distributions, ranging from 1.7 to 2.7 eV for thicknesses of 1.7 to 4 nm in the case SiQDs and from 3.5 to 1.1 eV for thicknesses of 1 to 7 nm in the case SiNWs.[28−30] In comparison, the SiNSs exhibited a wider range of band gaps (1.8 to 3.2 eV) for thicknesses ranging from 2 to 13 nm.

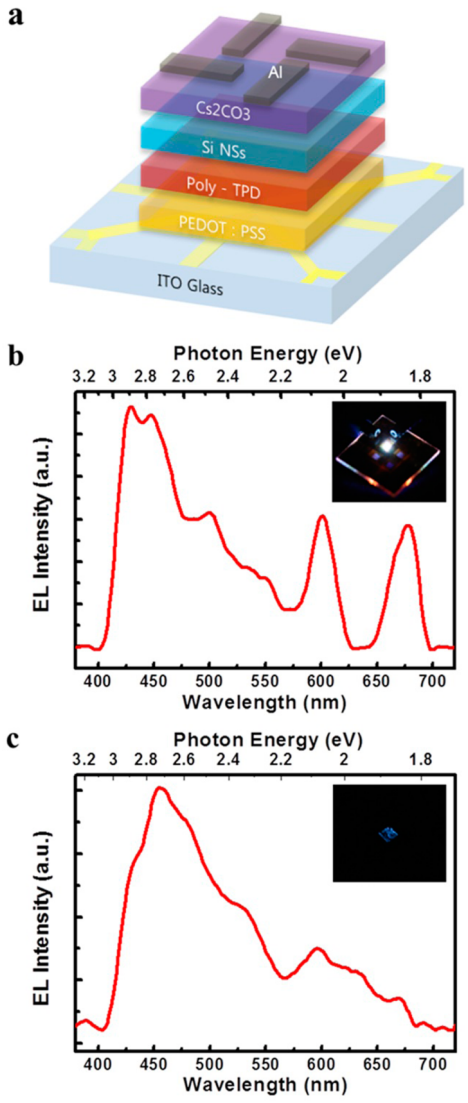


**Figure 4. Characterization of the SiNSs based OLEDs. (a) Schematic of the hybrid OLED fabricated using the SiNSs as the active layer. (b) Electroluminescence of mixtures of the SiNSs synthesized for growth times ranging from 1.5 to 20 min (c) Electroluminescence of the SiNSs synthesized for a growth time of 5 min.**

Figure 2 and Figure 3 show that, when Si grows in the form of 2D nanostructures, it can exhibit novel properties that can be exploited for numerous applications. For example, the unique optical properties of the synthesized SiNSs making them suitable for Si-based optoelectronic devices. The emissions from the SiNSs could be tuned readily in the visible range by altering the thickness of the SiNSs. This suggests that there is room for further optical engineering. For instance, white emissions, which usually require broad-spectrum radiation similar to that from the sun, could be achieved simply by mixing and using SiNSs synthesized for different growth times (*i.e.*, by using SiNSs having different thicknesses, Figure 2b).

To explore the potential of the SiNSs for use in Si-based optoelectronic devices, a SiNS-based organic light emitting diode (OLED) was fabricated. The device consisted of patterned indium tin oxide (ITO)/glass, poly(3,4-ethylenedioxythiophene) poly-(styrenesulfonate) (PEDOT:PSS) as the hole-injection layer (HIT), poly(4-butylphenyl-diphenyl-amine) (poly-TPD) as the hole-transporting layer (HTL), and $Cs_2CO_3$ QDs as the electron-injection layer (EIL) and the hole-blocking layer (HBL).[31] Figure 4 shows the structure of the OLED and the resulting electroluminescence (EL) spectrum. In this structure, the SiNSs were used as the active layer for light emission (Figure 4a). Figure 4b shows the EL from the OLED fabricated using SiNSs synthesized for growth times ranging from 1.5 to 20 min. The OLED exhibited white emission with peaks at 420, 480, 500, 530, 550, 600, and 615 nm. These wavelengths were similar to those of the PL emission peaks, demonstrating that the emission of white EL *via* the simple control of the thickness of the SiNSs was possible. Emissions of other wavelengths could also be achieved by varying the thickness of the SiNSs. For example, blue EL could be obtained from an OLED that used SiNSs synthesized for a growth time of 1.5 min (Figure 4c).

## CONCLUSIONS

In summary, we show the growth of free-standing, single-crystal SiNSs *via* CVD process. We propose a mechanism by which the high flow rate of gas suppresses the growth in ⟨111⟩ direction and results in 2D nanostructures *via* dendritic growth and filling mechanism in ⟨110⟩ direction. The SiNSs show thickness-dependent photoluminescence in a visible range of red, green, and blue with corresponding band gap energies of 1.8 to 3.2 eV, in keeping with the quantum confinement effect. The growth of the SiNSs demonstrates the feasibility of synthesizing 2D nanomaterials from nonlayered, isotropically structured materials. That the emissions from the SiNSs, whose wavelength varied as a function of the SiNS thickness, were tunable highlights the potential of the 2D nanostructures for use in a range of applications. For instance, along with their perfect single-crystalline nature, large surface area, and size tunability, the tunable emissions exhibited by the SiNSs make the nanostructures attractive for use in Si-based optoelectronic devices.

## MATERIALS AND METHODS

**Synthesis of SiNSs.** SiNSs were synthesized on a Si substrate *via* CVD. The substrates were cleaned using a conventional wet chemical method to remove any contaminations. The substrates were placed in the hot zone of a quartz tube reactor, and the reactor was heated to 1050 °C, with the atmosphere within the reactor of $H_2$; the flow rates were 200 to 5000 sccm, respectively. Silicon chloride ($SiCl_4$, 99.999%, Aldrich) was then bubbled into

the reactor using $H_2$ as the carrier gas at a flow rate of 1 to 50 sccm. These conditions were maintained for 1 to 120 min, and then the reactor was allowed to cool to room temperature

**Characterization of the SiNSs.** The morphologies of the SiNSs were observed using field emission scanning electron microscopy (FESEM, Hitachi 3000). The width of SiNSs was determined by observation of SiNSs grown on the substrates using SEM. The average of width was determined from more than hundred SiNSs. The thickness of SiNSs was determined by atomic force microscopy (AFM, Park system XE-100) that were dispersed on the substrates (Figure S8, Supporting Information). The average thickness was determined from at least 20 SiNSs. The structural characteristics were investigated using transmission electron microscopy (TEM, JEOL 7100, 200 keV). The PL spectra were measured for the as-grown SiNSs and the dispersed SiNSs in ethanol, respectively, using a He−Cd laser with a power of 3 mW and an excitation wavelength of 325 nm. The photocurrent from a single SiNS was measured at room temperature. And the thickness of single SiNS was determined by AFM (Figure S8f, Supporting Information). The photodetector was fabricated on a $SiO_2$ (100 nm)/p+ $SiO_2$ wafer and had Ti (20 nm)/Au (100 nm) ohmic contacts. Electron beam (e-beam) lithography and lift-off techniques were employed to fabricate the photodetector. The absorption coefficient ($\alpha$) and the optical band gap $E_g$ for the single SiNS based on the measured photocurrent were determined using the following equation:

$$\alpha = -\ln\left(1 - 1240\frac{R}{\lambda}\right)\frac{1}{w}\ [\mathrm{cm}^{-1}],\ \alpha h\nu \propto (h\nu - E_g)^n$$

Here, $R$ (= $I_{ph}/P_{hv}$) is the responsivity of a SiNS; $\lambda$ is the laser wavelength; $w$ is the SiNS thickness; and $n$ is 1/2 for a direct transition and 2 for an indirect transition. The optical band gap of the SiNS for a direct transition and for an indirect transition, $E_d$ and $E_i$, was determined by plotting $(\alpha h\nu)^2$ and $(\alpha h\nu)^{1/2}$, respectively, *versus* the photon energy. And, in case of photoluminescence, optical band gap of SiNSs were calculated using $E_g$ (in eV) = $hc/\lambda$ = 1.24/$\lambda$.

**Fabrication of a SiNS-Based OLED.** A SiNSs-based OLED with a multilayered *p-i-n* structure was assembled layer-by-layer using the spin coating method. A layer of patterned ITO/glass was used as the anode. A solution of the polymer PEDOT:PSS in isopropyl alcohol solution was spun, and the layer used as the HIT; the spun layer was annealed at 100 °C for 30 min. A solution of the polymer poly-TPD in chlorobenzene was spun to form the HTL; the layer was annealed for 20 min at 120 °C. A dispersion of the SiNSs in ethanol was spun to form the active layer, which was annealed at 120 °C for 20 min. A solution of $Cs_2CO_3$ in 2-ethoxyethanol was spun to form the EIL and the HBL; these layers were annealed at 90 °C for 10 min. Aluminum to form the cathode was deposited by thermal evaporation.

*Conflict of Interest:* The authors declare no competing financial interest.

*Acknowledgment.* This work was supported by a grant (No. 2012R1A2A1A03010558) and NRF-2011-Global Ph.D. Fellowship Program from the National Research Foundation (NRF) of Korea funded by the Ministry of Education, Science, and Technology (MEST), Korea. J. H. Sung and M.-H. Jo acknowledge the support by Institute for Basic Science (IBS), Korea under the contract number of CA1309.

*Supporting Information Available:* Additional SEM, TEM and AFM images of the SiNSs; structural characterization using XRD measurements; optical characterization using photocurrent device and data. This material is available free of charge *via* the Internet at http://pubs.acs.org.

## REFERENCES AND NOTES

1. Li, X.; Cai, W.; An, J. H.; Kim, S. Y.; Nah, J. H.; Yang, D. X.; Piner, R.; Velamakanni, A.; Jung, I. H.; Tutuc, E.; *et al.* Large-Area Synthesis of High-Quality and Uniform Graphene Films on Copper Foils. *Science* **2009**, *324*, 1312–1314.
2. Song, L.; Ci, L.; Lu, H.; Sorokin, P. B.; Jin, C. H.; Ni, J.; Kvasjnin, A. G.; Kvashnin, D. G.; Lou, J.; Yakobson, B. I.; *et al.* Large Scale Growth and Characterization of Atomic Hexagonal Boron Nitride Layers. *Nano Lett.* **2010**, *10*, 3209–3215.
3. Zhan, Y.; Liu, Z.; Najmaei, S.; Ajayan, P. M.; Lou, J. Large-Area Vapor-Phase Growth and Characterization of $MoS_2$ Atomic Layers on a $SiO_2$ Substrate. *Small* **2012**, *8*, 966–971.
4. Wang, S.; Qiao, L.; Zhao, C.; Zhang, X.; Chen, J.; Tian, H.; Zheng, W.; Han, Z. A Growth Mechanism for Graphene Deposited on Polycrystalline Co Film by Plasma Enhanced Chemical Vapor Deposition. *New J. Chem.* **2013**, *37*, 1616–1622.
5. Ozcelik, V. O.; Cahangirov, S.; Ciraci, S. Epitaxial Growth Mechanisms of Graphene and Effects of Substrates. *Phys. Rev. B: Condens. Matter Mater. Phys.* **2012**, *85*, 235456.
6. Wang, K.; Wamg, J.; Fan, J.; Lotya, M.; O'Neill, A.; Fox, D.; Feng, Y.; Zhang, X.; Jiang, B.; Zhao, Q.; *et al.* Ultrafast Saturable Absorption of Two-Dimensional $MoS_2$ Nanosheets. *ACS Nano* **2013**, *7*, 9260–9267.
7. Wang, X.; Zhi, C.; Weng, Q.; Bando, Y.; Golberg, D. Boron Nitride Nanosheets: Novel Syntheses and Applications in Polymeric Composites. *J. Phys.: Conf. Ser.* **2013**, *471*, 012003.
8. Lee, Y.-H.; Zhang, X.-Q.; Zhang, W.; Chang, M.-T.; Lin, C.-T.; Chang, K.-D.; Yu, Y.-C.; Wang, J. T. −W; Chang, C.-S.; Li, L.-J.; *et al.* Synthesis of Large-Area $MoS_2$ Atomic Layers with Chemical Vapor Deposition. *Adv. Mater.* **2012**, *24*, 2320–2325.
9. Guo, S.; Dong, S. Grahene Nanosheet: Synthesis, Molecular Engineering, Thin Film, Hybrids, and Energy and Analytical Applications. *Chem. Soc. Rev.* **2011**, *40*, 2644–2672.
10. Han, W.-Q.; Wu, L.; Zhu, Y.; Watanabe, W.; Taniguchi, T. Structure of Chemically Derived Mono- and Few-Atomic-Layer Boron Nitride Sheets. *Appl. Phys. Lett.* **2008**, *93*, 223103.
11. Bianconi, P. A.; Weidman, T. W. Poly(*n*-hexylsilyne): Synthesis and Properties of the First Alkyl Silicon $[RSi]_n$ Network Polymer. *J. Am. Chem. Soc.* **1988**, *110*, 2342–2344.
12. Okamoto, H.; Kumai, Y.; Sugiyama, Y.; Mitsuoka, T.; Nakanishi, K.; Ohta, T.; Nozaki, H.; Yamaguchi, S.; Shirai, S.; Nakano, H. Silicon Nanosheets and Their Self-Assembled Regular Stacking Structure. *J. Am. Chem. Soc.* **2010**, *132*, 2710–2718.
13. Lu, Z.; Zhu, J.; Sim, D.; Zhou, W.; Hnh, H. H.; Yan, Q. Synthesis of Ultrathin Silicon Nanosheets by Using Graphene Oxide as Template. *Chem. Mater.* **2011**, *23*, 5293–5295.
14. Okamoto, H.; Sugiyama, Y.; Nakano, H. Synthesis and Modification of Silicon Nanosheets and Other Silicon Nanomaterials. *Chem.—Eur. J.* **2011**, *17*, 9864–9887.
15. Kim, U. G.; Kim, I. S.; Park, Y. H.; Lee, K. Y.; Yim, S. Y.; Park, J. G.; Ahn, H. G.; Park, S. H.; Choi, H. J. Synthesis of Si Nanosheets by a Chemical Vapor Deposition Process and Their Blue Emissions. *ACS Nano* **2011**, *5*, 2176–2181.
16. Cartier, E.; Stathis, J. H.; Buchanan, D. A. Passivation and Depassivation of Silicon Dangling Bonds at the $Si/SiO_2$ Interface by Atomic Hydrogen. *Appl. Phys. Lett.* **1993**, *63*, 1510–1512.
17. Reider, G. A.; Hofer, U.; Heinz, T. F. Desorption Kinetics of Hydrogen from the Si(111) 7 × 7 Surface. *J. Chem. Phys.* **1991**, *94*, 4080–4083.
18. Niwano, M.; Terashi, M.; Kuge, J. Hydrogen Adsorption and Desorption on Si(100) and Si(111) Surfaces Investigated by *In Situ* Surface Infrared Spectroscopy. *Surf. Sci.* **1999**, *420*, 6–16.
19. Rivillon, S.; Amy, F.; Chabal, Y. J.; Frank, M. M. Gas Phase Chlorination of Hydrogen-Passivated Silicon Surfaces. *Appl. Phys. Lett.* **2004**, *85*, 2583–2585.
20. Libbrecht, K. G. The Physics of Snow Crystals. *Rep. Prog. Phys.* **2005**, *68*, 855–895.
21. Vicsek, T. Pattern Formation in Diffusion-Limited Aggregation. *Phys. Rev. Lett.* **1984**, *53*, 2281–2284.
22. Fan, H. J.; Scholz, R.; Kolb, F. M.; Zacharias, M.; Gosele, U.; Heyroth, F.; Eisenschmidt, C.; Hempel, T.; Christen, J. On the Growth Mechanism and Optical Properties of ZnO Multi-Layer Nanosheets. *Appl. Phys. A: Mater. Sci. Process.* **2004**, *79*, 1895–1900.
23. Li, C. P.; Lee, C. S.; Ma, X. L.; Wang, N.; Zhang, R. Q.; Lee, S. T. Growth Direction and Cross-Sectional Study of Silicon Nanowires. *Adv. Mater.* **2003**, *15*, 607–609.

24. Wu, Y.; Cui, Y.; Huynh, L.; Barrele, C. J.; Bell, D. C.; Liber, C. M. Controlled Growth and Structures of Molecular-Scale Silicon Nanowires. *Nano Lett.* **2004**, *4*, 433–436.
25. Park, J. H.; Choi, H.-J.; Choi, Y.-J.; Sohn, S. −H; Park, J.-G. Ultrawide ZnO Nanosheets. *J. Mater. Chem.* **2004**, *14*, 35–36.
26. Fauchet, P. M. Light Emission from Si Quantum Dots. *Mater. Today* **2005**, *8*, 26–33.
27. Takeoka, S.; Fujii, M.; Hayashi, S. Size-Dependent Photoluminescence from Surface-Oxidized Si Nanocrystals in a Weak Confinement Regime. *Phys. Rev. B: Condens. Matter Mater. Phys.* **2000**, *62*, 16821–16825.
28. Dohnalova, K.; Poddubny, A. N.; Prokofiev, A. A.; Boer, W. D.; Umesh, C. P.; Paulsse, J. M.; Zuilhof, H.; Gregorkiewicz, T. Surface Brightens up Si Quantum Dots: Direct Bandgap-Like Size-Tunable Emission. *Light: Sci. Appl.* **2013**, *2*, e47.
29. Yu, H.; Li, J.; Loomis, R. A.; Wang, L. −W; Buhro, W. E. Two- *Versus* Three-Dimensional Quantum Confinement in Indium Phosphide Wires and Dots. *Nat. Mater.* **2013**, *21*, 517–520.
30. Ma, D. D. D.; Lee, C. S.; Au, F. C. K.; Tong, S. Y.; Lee, S. T. Small-Diameter Silicon Nanowire Surfaces. *Science* **2003**, *299*, 1874–1877.
31. Son, D. I.; Kwon, B. W.; Park, D. H.; Seo, W.-S.; Yi, Y. J.; Angadi, B.; Lee, C.-L.; Choi, W. K. Emissive ZnO-Graphene Quantum Dots for White-Light-Emitting Diodes. *Nat. Nano.* **2012**, *7*, 465–471.